Electronic Supplementary Material (ESI) for Sensors & Diagnostics.
This journal is © The Royal Society of Chemistry 2023

Supporting Information for

Functionalized metal-organic frameworks based on multi-catalysts ordered assembly for electrochemical stripping chemiluminescent immunoassay

Xu Liang, Yuecong Hu, Xinhe Zheng, Yi Shao, Yutong Hua, Junjie Liu, Zhiwei Zhu & Yuanhua Shao*

Beijing National Laboratory for Molecular Sciences, College of Chemistry and Molecular Engineering, Peking University, Beijing 100871, China

*Email: yhshao@pku.edu.cn

Preparation of Cu-Hemin MOFs and Au@MOFs

As shown in Scheme S1. In neutral buffer, the three-dimensional structure of Cu-Hemin MOFs were first generated through the coordination between Cu^{2+} and the carboxyl groups of Hemin molecules. Subsequently, a large number of negatively charged AuNPs were loaded into the open pores of Cu-Hemin MOFs through the electrostatic interaction to obtain Au@MOFs.

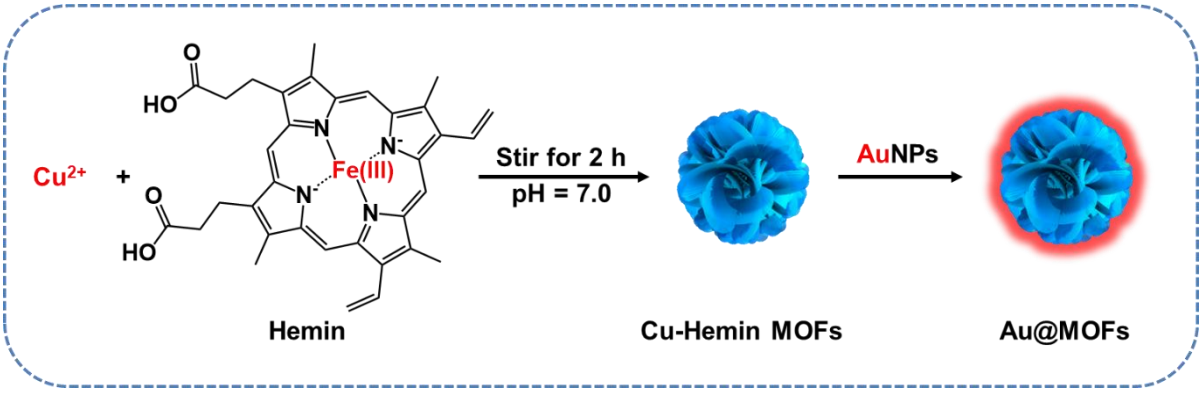

Scheme S1 Schematic illustration of the preparation of Cu-Hemin MOFs and Au@MOFs.

Comparison of element contents between Cu-Hemin MOFs and Au@MOFs

Compared with Cu-Hemin MOFs, the content of element Au in Au@MOFs increases significantly, as shown in Table S1.

Table S1 A comparison of quantitative element contents between Cu-Hemin MOFs and Au@MOFs.

	Element	C K	N K	O K	Fe K	Cu K	**Au L**
Cu-Hemin MOFs	Weight (%)	28.34	1.87	48.32	1.87	19.06	**0.54**
	Atomic (%)	40.34	2.28	51.63	0.57	5.13	**0.05**
Au@MOFs	Weight (%)	20.36	1.76	47.94	1.29	10.76	**17.88**
	Atomic (%)	33.23	2.47	58.75	0.45	3.32	**1.78**

Characterization of Cu-Hemin MOFs and Au@MOFs by UV-vis absorption spectra

UV-Vis absorption spectra were used to analyze the composition of the synthesized materials, as shown in Fig. S1. In Cu-Hemin MOFs, the characteristic absorption peak of Cu^{2+} disappears, only weak B band absorption of Hemin can be observed at 410 nm,[S1] which demonstrates that the small-sized Cu^{2+} is inserted into the larger Hemin molecules in an atomic-level dispersed state.[S2] In the mixture of Cu-Hemin MOFs and AuNPs, the absorption peaks of B band (404 nm) and AuNPs (524 nm) can be observed at the same time with no significant peak shift, while in Au@MOFs, the absorption peak of AuNPs disappears, indicating that AuNPs were successfully loaded into Cu-Hemin MOFs, consistent with the results of EDAX.

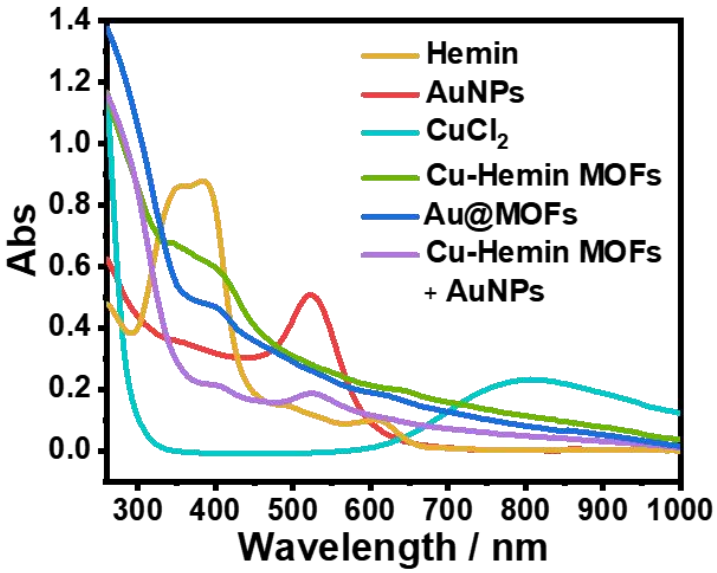

Fig. S1 UV absorption spectra of Hemin (yellow curve), AuNPs (red curve), $CuCl_2$ (Cyan curve), Cu-Hemin MOFs (green curve), Au@MOFs (blue curve), and the mixture of Cu-Hemin MOFs and AuNPs (purple curve).

Characterization of Cu-Hemin MOFs and Au@MOFs by XRD spectra

XRD spectra were used to characterize the chemical composition and crystal phase purity of the synthesized materials, as shown in Fig. S2. In the XRD spectrum of Cu-Hemin MOFs, significant diffraction peaks can be observed around 8.1, 12.8, 20.8, 29.9, 33.5, 40.1, and 53.2°, indicating that the three-dimensional flower spherical structure has good crystallinity.[S1, S3] In the XRD spectrum of Au@MOFs, the diffraction peaks of Cu-Hemin MOFs are basically unchanged, and new diffraction peaks appear around 38.2 and 44.3°, representing the (111) and (200) crystal planes of AuNPs, respectively, indicating that AuNPs were successfully loaded into Cu-Hemin MOFs with the retained three-dimensional structure of MOFs, consistent with the characterization results of SEM.

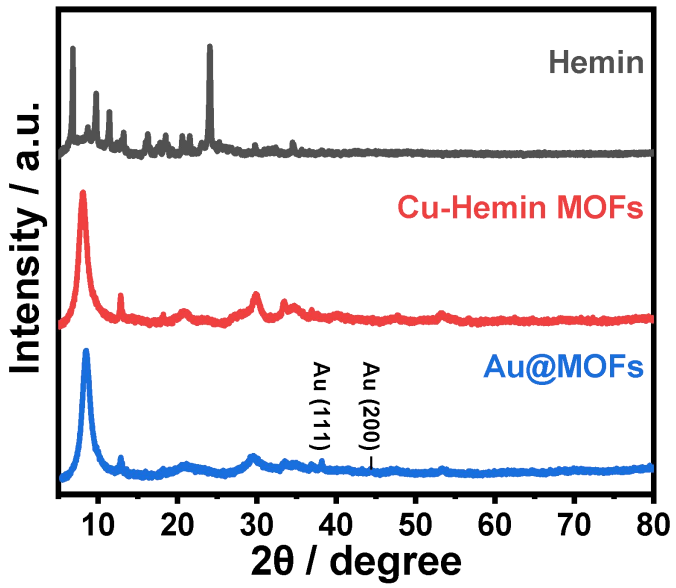

Fig. S2 The XRD spectra of Hemin (black curve), Cu-Hemin MOFs (red curve), and Au@MOFs (blue curve), respectively.

The high resolution XPS spectra of Hemin, Cu-Hemin MOFs, and Au@MOFs

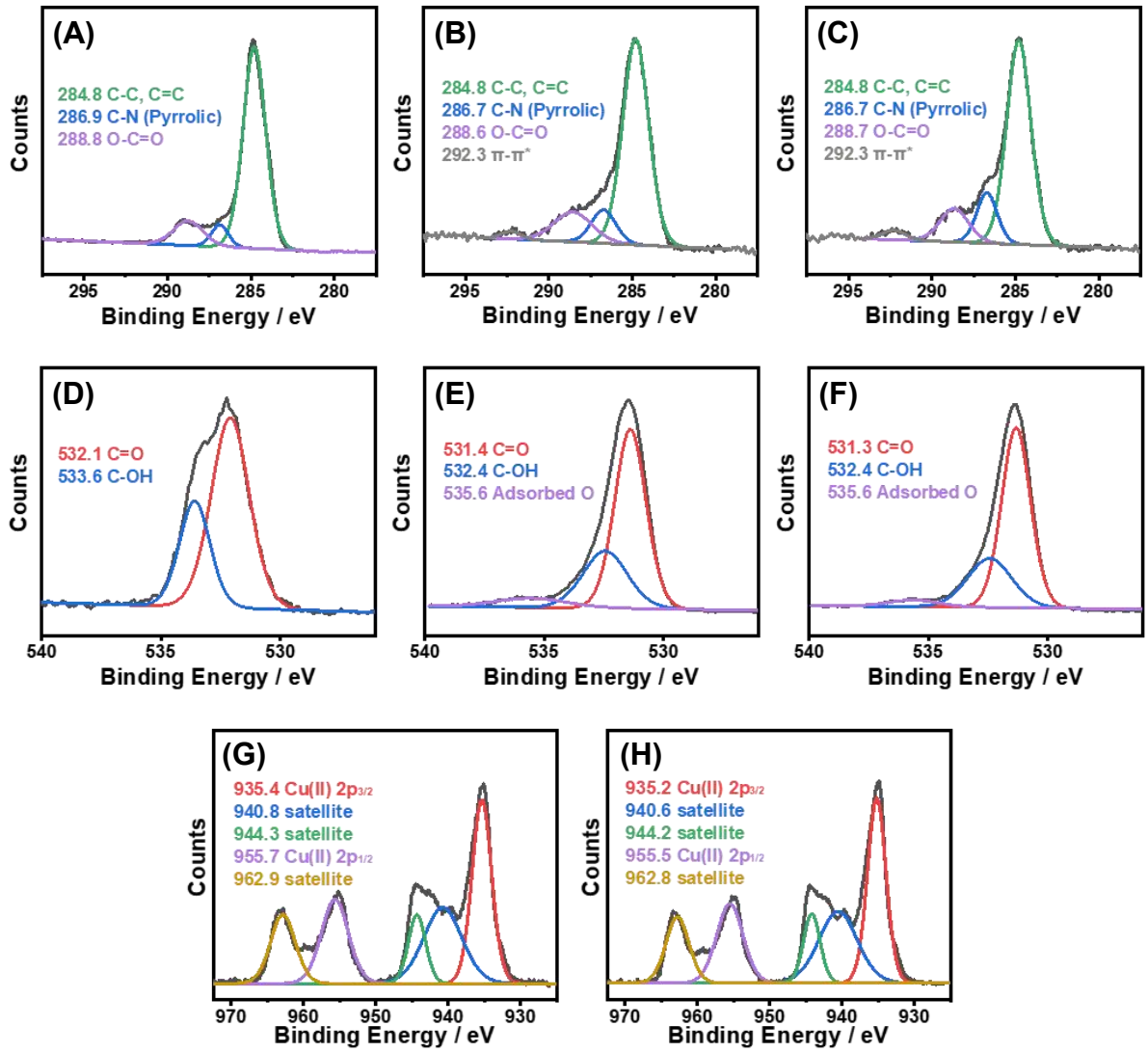

Fig. S3 The high resolution XPS spectra of C 1s of Hemin (A), Cu-Hemin MOFs (B), and Au@MOFs (C), respectively. The high resolution XPS spectra of O 1s of Hemin (D), Cu-Hemin MOFs (E), and Au@MOFs (F), respectively. The high resolution XPS spectra of Cu 2p of Cu-Hemin MOFs (G) and Au@MOFs (H).

ESCL process

After the synthesized Au@MOFs were modified on the electrode surface and a certain potential range was applied (−1.0 ~ 1.0 V), Cu^{2+} gradually dissolved from the electrode surface, and then cooperated with Hemin and AuNPs in the MOF composites to catalyze the ECL reaction, resulting a triple amplified ESCL process, as shown in Scheme S2.

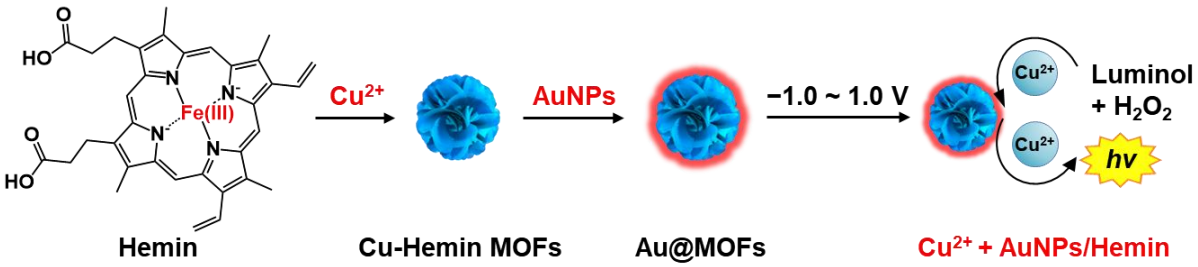

(1) Anodic stripping: $Au@MOFs - 2e^- \rightarrow Cu^{2+} + AuNPs/Hemin$

(2) ECL: $luminol + H_2O_2 \xrightarrow[AuNPs/Hemin]{Cu^{2+}} luminol[O] + hv$

Scheme S2 Schematic illustration of the ESCL process of luminol-H_2O_2/Au@MOFs system.

ECL catalytic amplification mechanism

Representative catalysts were selected for the electrode modification and CV scanning to explore the catalytic amplification mechanism towards the ECL intensity of the luminol-H_2O_2 system (Fig. S4).

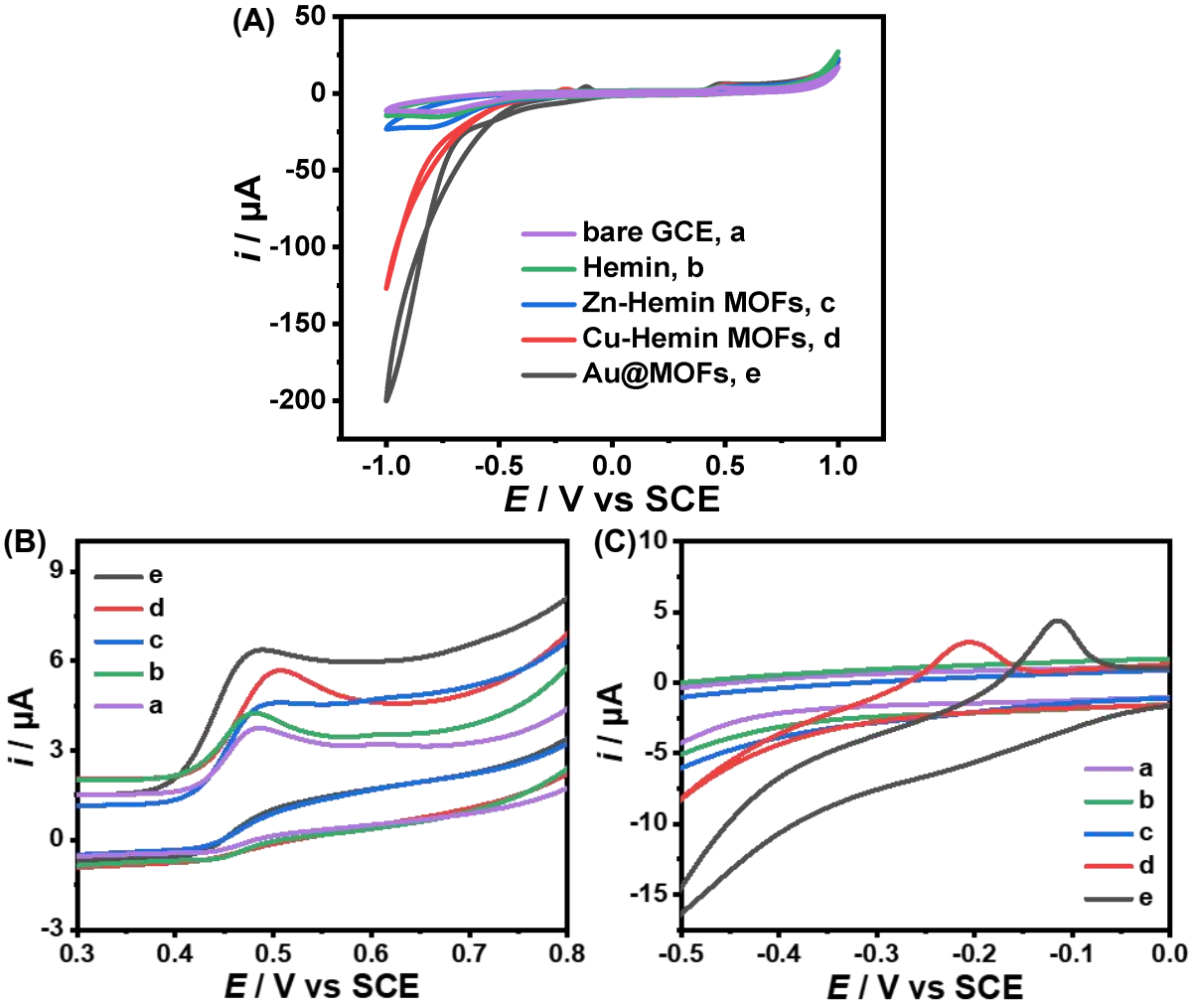

Fig. S4 (A) CV of bare GCE (purple curve, a), Hemin (green curve, b), Zn-Hemin MOFs (blue curve, c), Cu-Hemin MOFs (red curve, d) and Au@MOFs (black curve, e) modified GCE in 0.1 M PBS (pH = 7.4) containing 100 μM luminol and 10 mM H_2O_2. Scan rate: 0.1 V/s. Scan potential: −1.0 ~ +1.0 V. (B) The magnification of (A) from 0.3 V to 0.8 V. (C) The magnification of (A) from −0.5 V to 0 V.

With the layer-by-layer assembly of the structural units, the reduction peak of H_2O_2 right shifts with the increased peak current (Fig. S4A), while the oxidation peak of luminol is basically unchanged, only the peak current increases slightly (Fig. S4B). These results demonstrate that the ordered assembly of multiple catalysts can significantly improve the electron transport efficiency and accelerate the conversion of H_2O_2 to reactive oxygen

species (ROS), so that the electrooxidized luminol anions can be rapidly converted into high-energy excited states to produce stronger ECL emission, as shown in equations S1−S4.

$$H_2O_2 + e^- \rightarrow ROS \quad (S1)$$

$$luminol^- - e^- \rightarrow luminol^{\cdot -} + H^+ \quad (S2)$$

$$luminol^{\cdot -} + ROS \rightarrow luminol[O]^* \quad (S3)$$

$$luminol[O]^* \rightarrow luminol[O] + h\nu \quad (S4)$$

It is worth noting that, for Cu-Hemin MOFs and Au@MOFs, significant Cu^{2+} stripping peaks can be observed around −0.2 V and −0.1 V, respectively.[S4] The latter peak shape was sharper with higher peak current (Fig. S4C), indicating that the assembly of AuNPs can significantly improve the detection sensitivity.

ECL performance optimization

In order to obtain the best ECL signal response, it is necessary to explore the influence of each component content in the Au@MOFs on the ECL signal of the luminol-H_2O_2 system. The ECL signals of 10.00 μL of different concentrations of Cu-Hemin MOFs modified GCE in luminol-H_2O_2 system were first explored, as shown in Fig. S5A and S5B. The best concentration of Cu-Hemin MOFs dispersion should be 5.0 μM. Then, the effect of adding different volumes of Na_3Cit@AuNPs to 1.0 mL Cu-Hemin MOFs dispersion on the ECL signal of the system was explored (Fig. S5C and S5D), and 1.0 mL of Na_3Cit@AuNPs should be added to the Cu-Hemin MOFs dispersion.

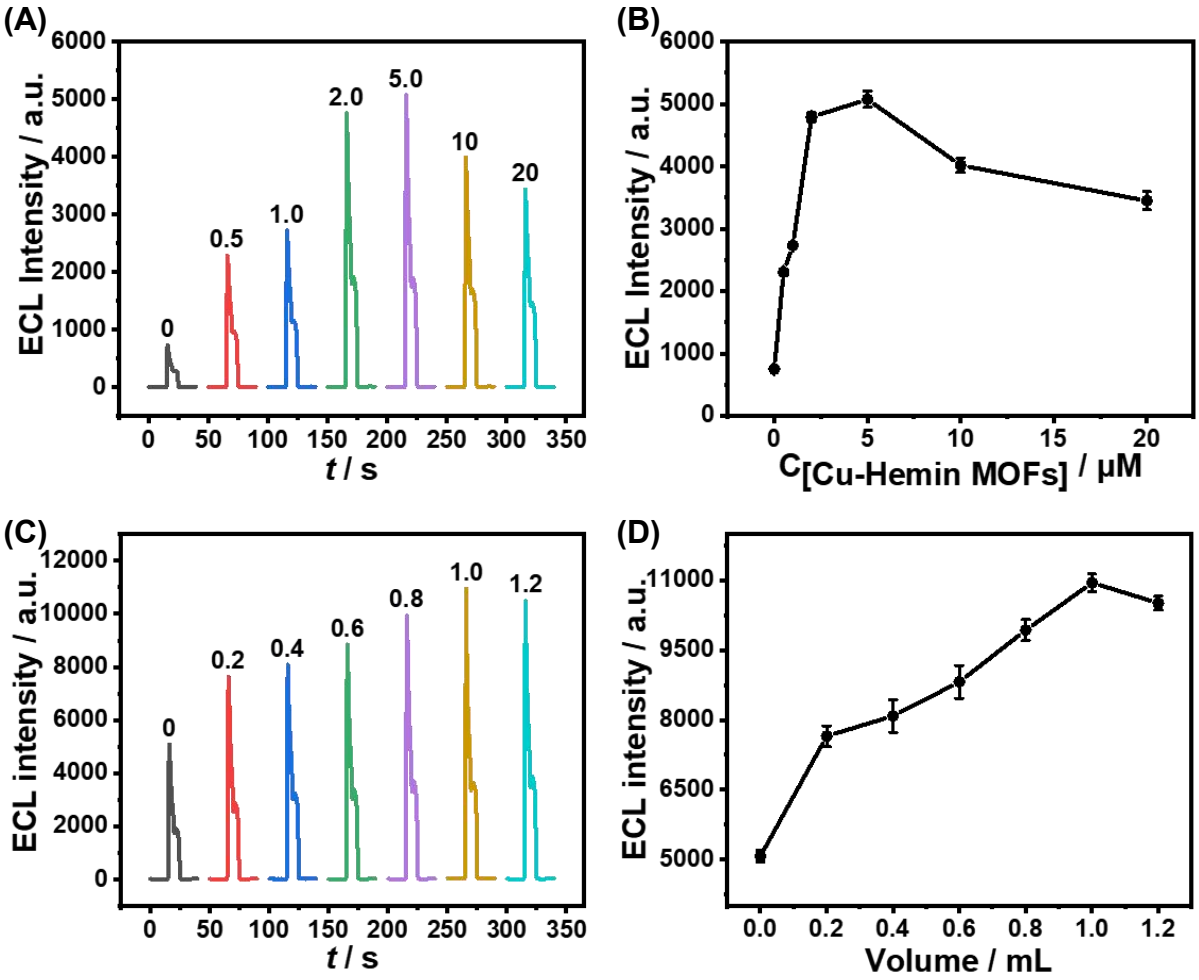

Fig. S5 ECL response of Cu-Hemin MOFs modified GCE (A) and the corresponding curve of ECL intensity to different concentrations of Cu-Hemin MOFs (B). ECL response of Au@MOFs modified GCE (C) and the corresponding curve of ECL intensity to different volume of Na_3Cit@AuNPs added in 1 mL Cu-Hemin MOFs (D). All the experiments were conducted in 0.1 M PBS (pH = 7.4) containing 100 μM luminol and 10 mM H_2O_2. Scan rate: 0.1 V/s. Scan potential: −1.0 ~ +1.0 V. PMT = 600 V.

Characterization of ESCL immunosensor

As shown in Fig. S6, the electrochemical characterizations of the fabricated ESCL immunosensor, including cyclic voltammetry (CV) and electrochemical impedance spectroscopy (EIS), were carried out step by step in $Fe(CN)_6^{3-/4-}$ solution.

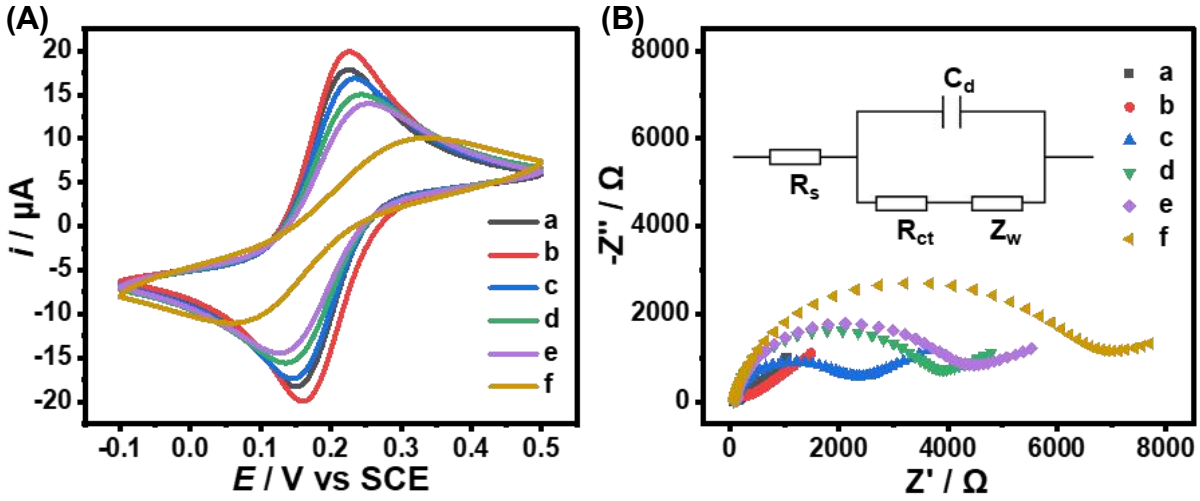

Fig. S6 CV (A) and EIS (B) of the modified electrodes during ESCL immunosensor assembly. (a) bare GCE, (b) Au_{plate}/GCE, (c) anti-cTnI/Au_{plate}/GCE, (d) BSA/anti-cTnI/Au_{plate}/GCE, (e) cTnI/BSA/anti-cTnI/Au_{plate}/GCE, and (f) anti-cTnI-Au@MOFs/cTnI/BSA/anti-cTnI/Au_{plate}/GCE. All the experiments were conducted in 0.1 M PBS (pH = 7.4) containing 1.0 mM $K_4Fe(CN)_6$ and 1.0 mM $K_3Fe(CN)_6$. Scan rate: 0.05 V/s. EIS: 100−1 Hz, 5 mV rms, 0.21 V vs SCE. cTnI concentration: 0.10 ng/mL.

Optimization of the detection conditions of ESCL sensor

To achieve the most sensitive ECL response, the influence of the incubation time of anti-cTnI-Au@MOFs on the ECL signal was explored, as shown in Fig. S7A and S7B. Considering the time cost and the detection sensitivity, 40 min was selected as the optimal incubation time. In addition, the pH value of the detection solution is also one of the important factors affecting the results of immunoassays. The ECL response of immunoelectrodes in the neutral pH range was mainly explored, as shown in Fig. S7C and S7D. Considering the high ECL response and the low chemiluminescence background, 7.4 was selected as the most suitable pH value.

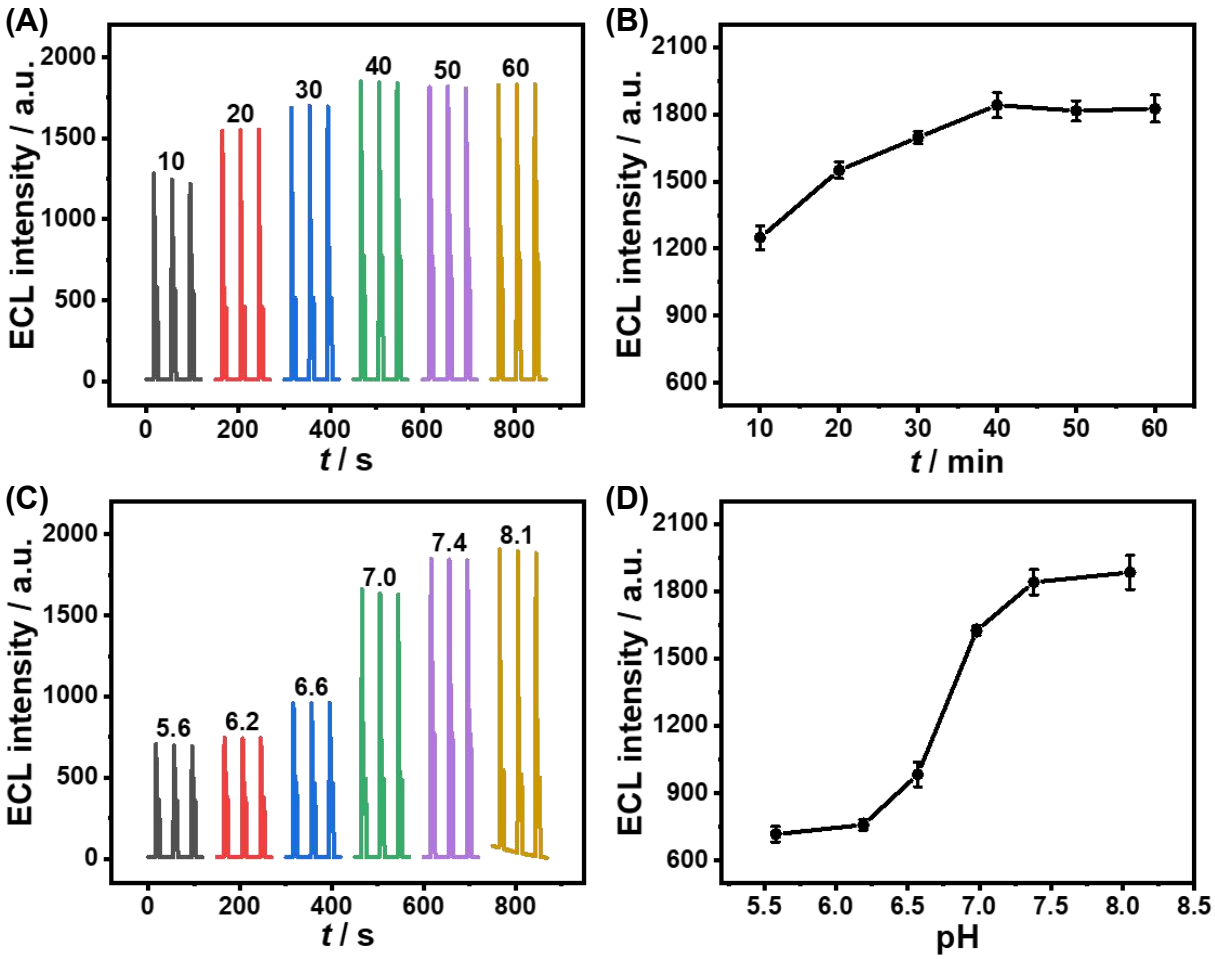

Fig. S7 ECL response of the ESCL immunosensor (A) and the corresponding curve of ECL intensity to different incubation time of anti-cTnI-Au@MOFs (B). ECL response of the ESCL immunosensor (C) and the corresponding curve of ECL intensity to different pH value of the detection buffer (D). All the experiments were conducted in 0.1 M PBS containing 100 μM luminol and 10 mM H_2O_2. cTnI concentration: 0.10 ng/mL. Scan rate: 0.1 V/s. Scan potential: −1.0 to +1.0 V. PMT = 600 V.

Analytical performance Comparison

As shown in Table S2, the sensitivity of the fabricated ESCL sensor is competitive with or better than those of other previous reports.

Table S2 Comparison of the fabricated ESCL sensor with other immunosensors.

Analyte	Analytical method	Label	Sensing platform	LDR (ng/mL)	LOD (pg/mL)	Ref
cTnI	SWV	Label	TdT-aptamer-probe	0.5−100	40	S5
	DPV	Label-free	Cu-MOF-74/NH_2-rGO	1.0×10^{-5}−1.0	4.5×10^{-3}	S6
	Digital Count	Label	AuNPs	5×10^{-3}−5	1.4	S7
	SERS	Label	Au-4MBA@Ag	0−2	9.8	S8
	PEC	Label-free	SiNWs@PDA	0.005−10	1.47	S9
	PEC	Label	Zr-MOF@TiO_2NRs	0.01−10	8.6	S10
	CL	Label-free	CS-Co^{2+}-Luminol-Au	0.01−10000	1.57	S11
	ECL	Label-free	TEOA@Au	3.50×10^{-4}–350	3.4×10^{-2}	S12
	ECL	Label	MoS_2@Cu_2O–Ag	0.01−100	2.9×10^{-3}	S13
	ESCL	Label-free /Label	fullerenol@AuNPs	3.50×10^{-4}–350 /3.5×10^{-6}–35	3.7×10^{-2} /1.5×10^{-3}	S14
	ESCL	Label	Au@MOFs	1.0×10^{-5}–1.0×10^{2}	7.8×10^{-4}	This work

TdT: terminal deoxynucleotidyl transferase. NH_2-rGO: amino groups functionalized reduced graphene oxide. 4MBA: 4-mercaptobenzoic acid. PEC: photoelectrochemistry. SiNWs: silicon nanowires. PDA: polydopamine. TEOA: triethanolamine

References

S1. J. He, H. Yang, Y. Zhang, J. Yu, L. Miao, Y. Song and L. Wang, *Sci. Rep.*, 2016, **6**, 36637.

S2. H. S. Choi, X. Yang, G. Liu, D. S. Kim, J. H. Yang, J. H. Lee, S. O. Han, J. Lee and S. W. Kim, *J. Taiwan Inst. Chem. Eng.*, 2020, **113**, 1-7.

S3. X. Chen, X. Wang, G. Cao, Y. Wu, H. Luo, Z. Ji, C. Shen, D. Huo and C. Hou, *Microchim. Acta*, 2020, **187**, 601.

S4. T. Liu, R. Hu, X. Zhang, K. Zhang, Y. Liu, X. Zhang, R. Bai, D. Li and Y. Yang, *Anal. Chem.*, 2016, **88**, 12516-12523.

S5. M. Lang, D. Luo, G. Yang, Q. Mei, G. Feng, Y. Yang, Z. Liu, Q. Chen and L. Wu, *RSC Adv.*, 2020, **10**, 36396-36403.

S6. Y. Ling, Y. R. Chu, F. Gao, Q. Y. Feng, H. Q. Xie, Y. Shao and Q. X. Wang, *J. Phys. Chem. C*, 2022, **126**, 9416-9424.

S7. Y. Wang, Y. Yang, C. Chen, S. Wang, H. Wang, W. Jing and N. Tao, *ACS Sens.*, 2020, **5**, 1126-1131.

S8. C. Hu, L. Ma, F. Mi, M. Guan, C. Guo, F. Peng, S. Sun, X. Wang, T. Liu and J. Li, *New J. Chem.*, 2021, **45**, 3088-3094.

S9. H. J. Li, S. Zhi, S. Zhang, X. Guo, Y. Huang, L. Xu, X. Wang, D. Wang, M. Zhu and B. He, *Biomater. Sci.*, 2022, **10**, 4627-4634.

S10. Y. Gao, M. Li, Y. Zeng, X. Liu and D. Tang, *Anal. Chem.*, 2022, **94**, 13582-13589.

S11. F. Li, A. Zhao, Z. Li, Y. Xi, J. Jiang, J. He, J. Wang and H. Cui, *Anal. Chem.*, 2022, **94**, 2665-2675.

S12. X. Qin, C. Gu, M. Wang, Y. Dong, X. Nie, M. Li, Z. Zhu, D. Yang and Y. Shao, *Anal. Chem.*, 2018, **90**, 2826-2832.

S13. B. Wang, C. Wang, Y. Li, X. Liu, D. Wu and Q. Wei, *Analyst*, 2022, **147**, 4768-4776.

S14. Y. Dong, X. Qin, M. Wang, C. Gu, Z. Zhu, D. Yang and Y. Shao, *Anal. Chem.*, 2020, **92**, 1890-1897.